Supplement of Atmos. Chem. Phys., 22, 14489–14502, 2022
https://doi.org/10.5194/acp-22-14489-2022-supplement

Atmospheric Chemistry and Physics
Open Access
EGU

Supplement of

Dust pollution in China affected by different spatial and temporal types of El Niño

Yang Yang et al.

Correspondence to: Yang Yang (yang.yang@nuist.edu.cn)

Text S1. Mechanisms of different types of El Niño

The EP El Niño is associated with basin-wide thermocline and surface wind variations and shows a strong teleconnection with the tropical Indian Ocean. In contrast, the CP El Niño appears less related to the thermocline variations and may be influenced more by atmospheric forcing. It has a stronger teleconnection with the southern Indian Ocean (Kao and Yu, 2009). Base on this, many studies have found that EP and CP El Niño cause different atmospheric circulation. Yuan and Yang (2012) pointed that the East Asia winter monsoon is weaker (stronger) during the winter of EP (CP) El Niño. Yu et al. (2020) noted that there are obvious southerly (northerly and northwesterly) wind anomalies at the middle to lower troposphere over eastern China during the winter of EP (CP) El Niño. These are consistent with the results in our study. The thermocline during LD El Niño mature phase is relatively shallower than that of SD El Niño. Moreover, the SST anomalies of SD El Niño are larger than LD El Niño, and the different depths of the thermocline indicates large differences in the recharged energy going into the eastern Pacific, which may lead to different oceanic and atmospheric conditions during their decaying periods (Guo and Tan, 2018). As for EP and CP El Niño, the SST anomaly centers are located in the eastern and central equatorial Pacific, respectively. The different locations of the SSTA generate differences in atmospheric circulation anomalies. As for SD and LD El Niño, the locations of the SST anomalies are similar, but LD El Niño has a longer duration and weaker intensity, thus generating different atmospheric circulations.

Table S1. The classification of different spatial and temporal types El Niño events

Spatial Types		Temporal Types	
Eastern Pacific El Niño	Central Pacific El Niño	Short Duration El Niño	Long Duration El Niño
1877/1878,	1885/1886,	1877/1878, 1885/1886,	1899/1900,
1888/1889,	1968/1969,	1888/1889, 1896/1897,	1904/1905,
1896/1897,	1977/1978,	1902/1903, 1911/1912,	1913/1914,
1899/1900,	1994/1995,	1923/1924, 1925/1926,	1918/1919,
1902/1903,	2002/2003,	1930/1931, 1951/1952,	1939/1940,
1904/1905,	2004/2005,	1957/1958, 1963/1964,	1968/1969,
1911/1912,	2009/2010,	1965/1966, 1972/1973,	1976/1977,
1913/1914,	2014/2015.	1982/1983, 1991/1992,	1986/1987.
1914/1915,		1994/1995, 1997/1998,	
1918/1919,		2002/2003, 2006/2007,	
1923/1924,		2009/2010, 2015/2016.	
1925/1926,			
1930/1931,			
1939/1940,			
1951/1952,			
1957/1958,			
1963/1964,			
1965/1966,			
1972/1973,			
1976/1977,			
1982/1983,			
1986/1987,			
1991/1992,			
1997/1998,			
2006/2007.			

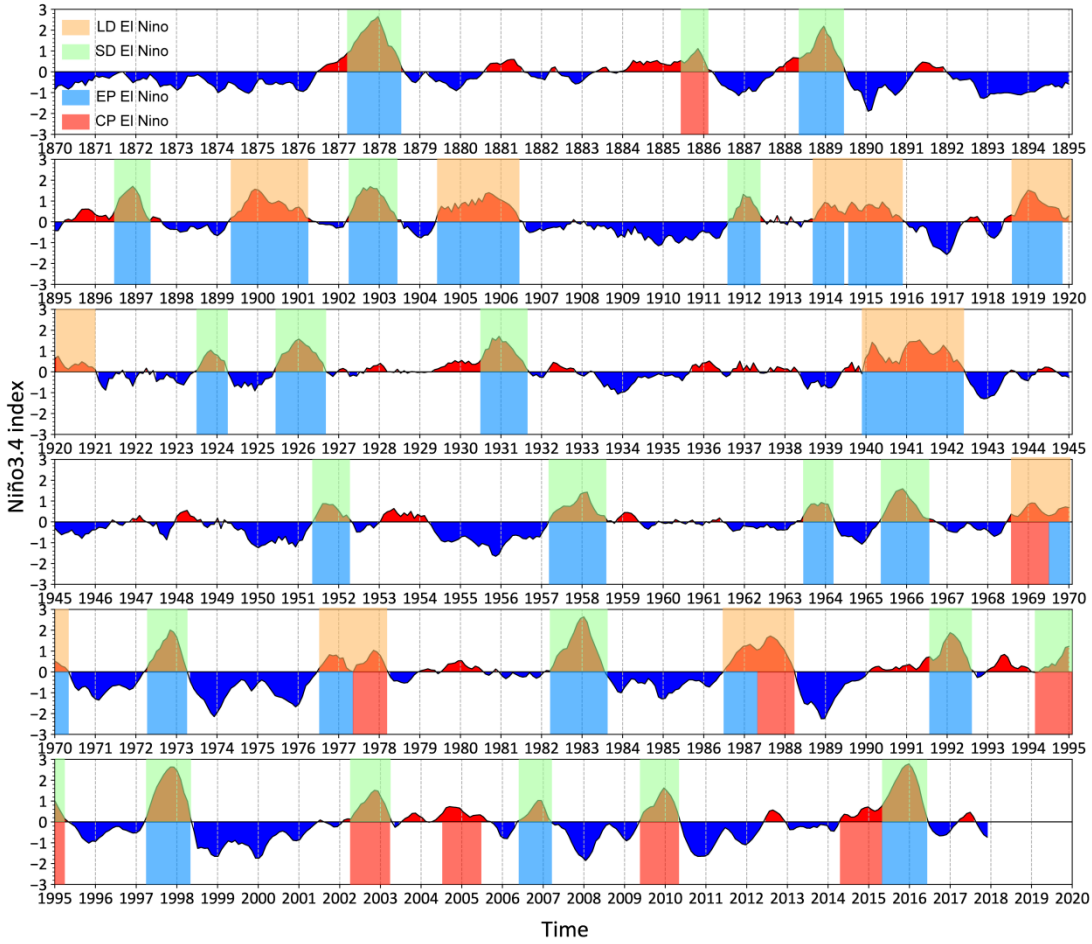

Figure S1. Time series of the Niño3.4 index (°C) based on the merged Hadley-NOAA/OI SST dataset for 1870–2017. The time series were detrended and smoothed with a 3-month running average filter. Highlighted slots illustrate the EP (blue), CP (red), SD (green) and LD (orange) El Niño events.

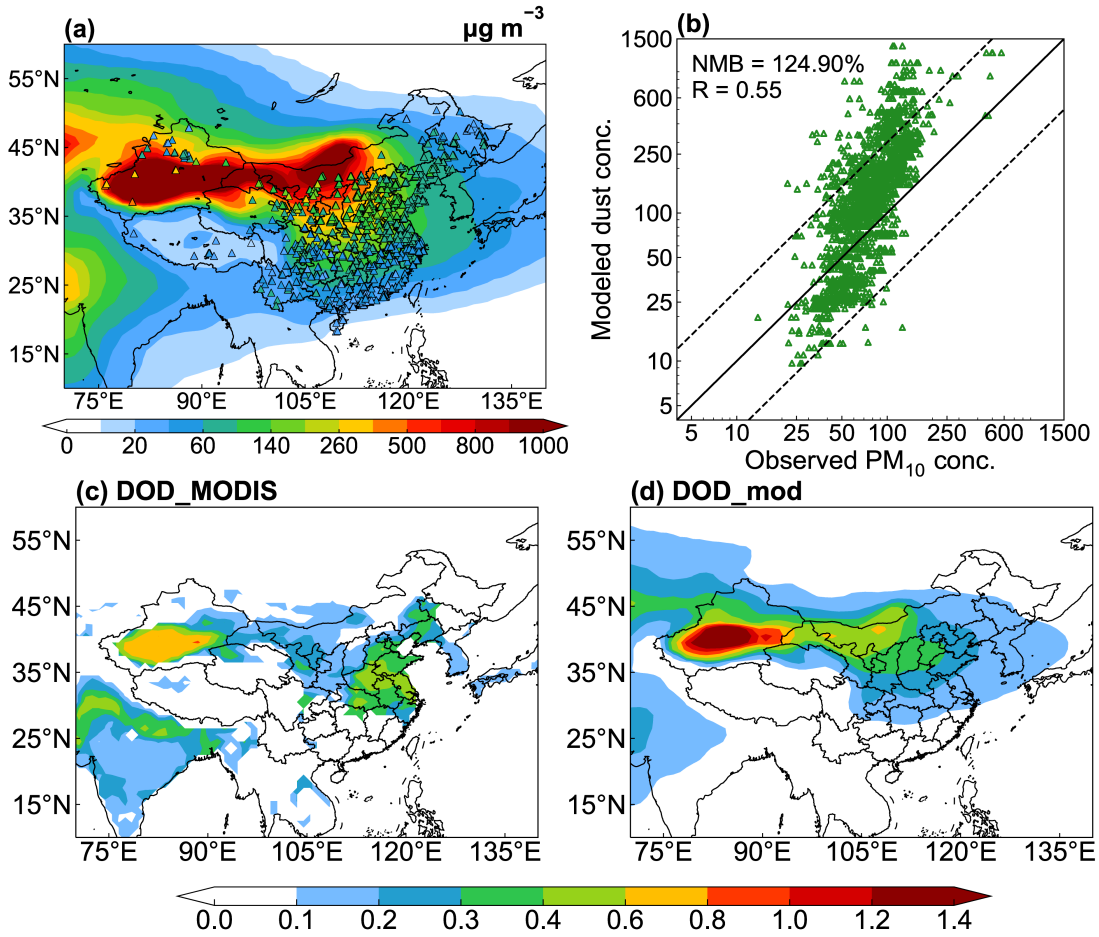

Figure S2. Spatial distributions (a) and scatter plots (b) of MAM mean observed near-surface PM_{10} concentrations (μg m^{-3}, color-filled triangles in a) and simulated dust concentrations (μg m^{-3}, contour in a) from the CLIM experiment. Solid line represents 1:1 ratio and dashed lines mark 1:3 and 3:1 ratios. The observed concentrations are derived from the CNEMC in 2015–2021. The normalized mean deviation (NMB) and the correlation coefficient (R) between observations and simulation are shown in the upper left corner of (b). NMB = 100% × $\sum(M_i - O_i)/\sum O_i$, where M_i and O_i are the simulated and observed values at the site i, respectively. Spatial distributions of MAM mean Dust Optical Depth (DOD) from MODIS over 2001–2020 and CLIM experiment are shown in (c) and (d), respectively.

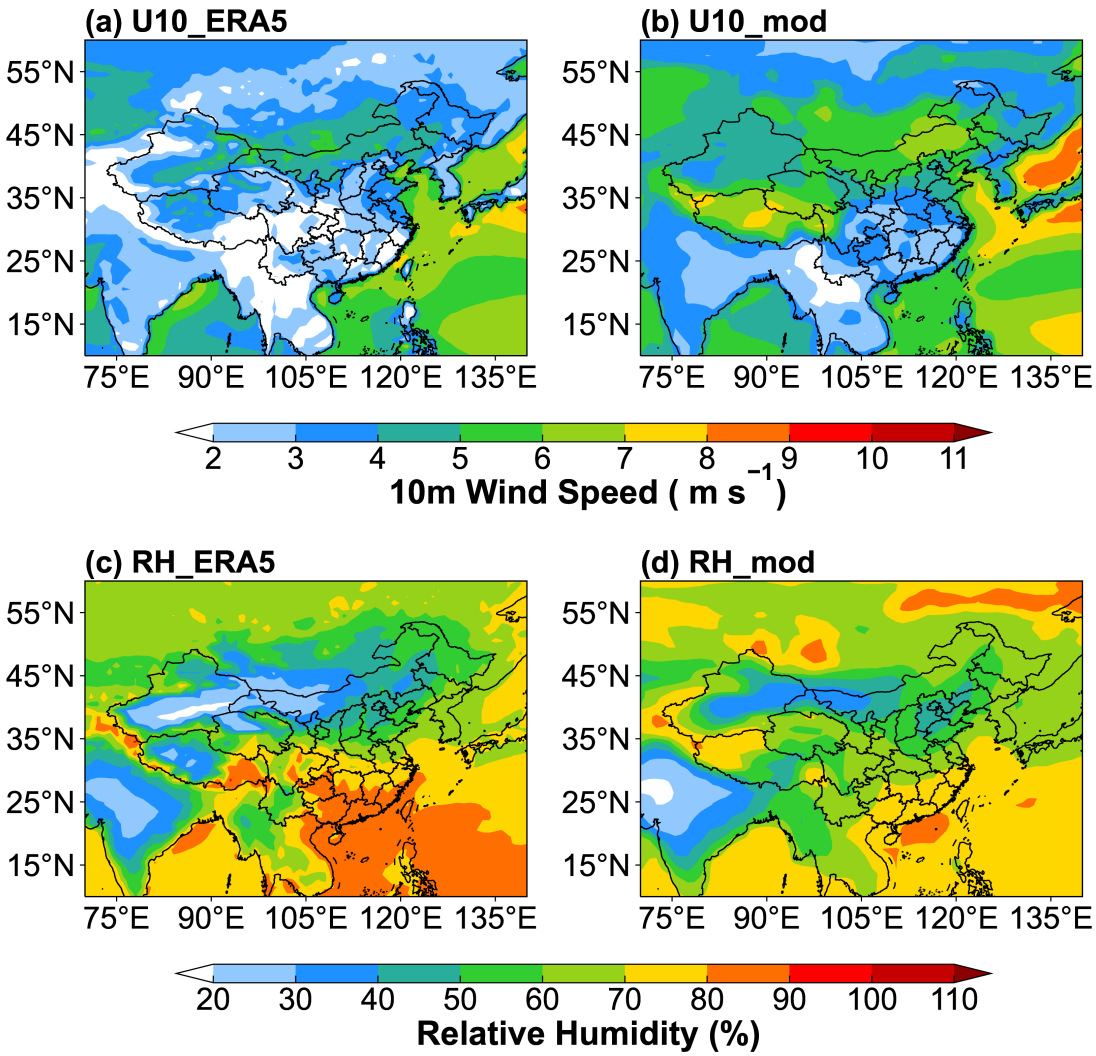

Figure S3. Spatial distributions of MAM mean 10-m wind speed (m s^{-1}) (top panels) and relative humidity (units: %, bottom panels) from ERA5 over 1950–2020 in (a) and (c) and CLIM experiment in (b) and (d), respectively.

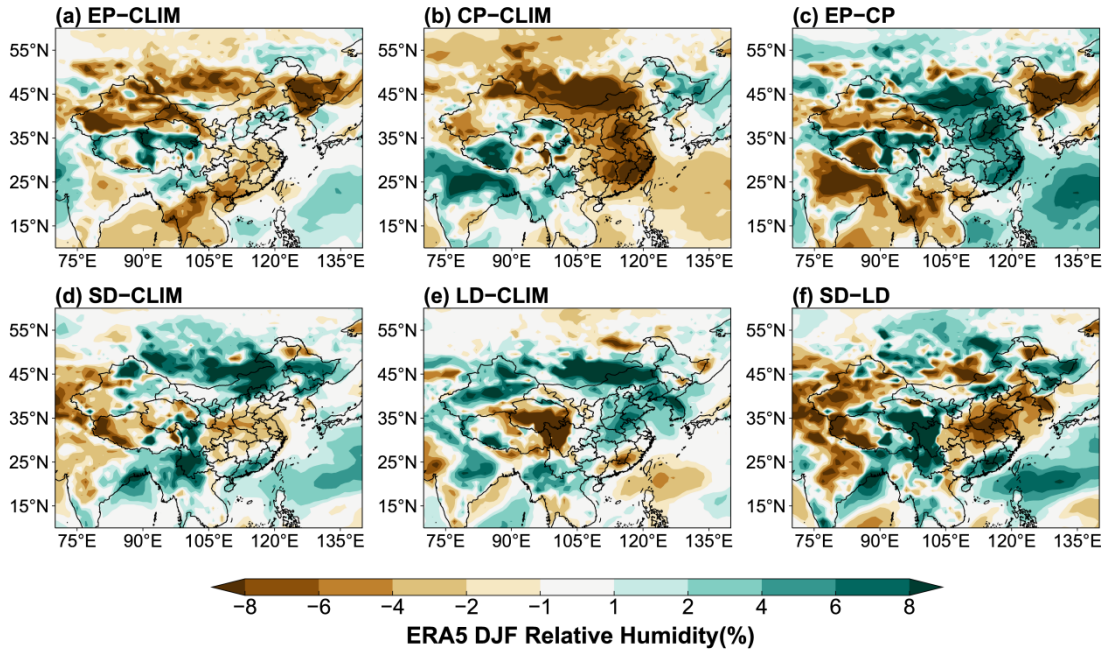

Figure S4. Composite differences in DJF mean relative humidity (units: %) between 2006/07 EP El Niño and climatological mean (1950–2017) in (a), 2014/15 CP El Niño and climatological mean in (b), 2006/07 EP El Niño and 2014/15 CP El Niño in (c), 2015/16 SD El Niño and climatological mean in (d), 1986/87 LD El Niño and climatological mean in (e), 2015/16 SD El Niño and 1986/87 LD El Niño in (f) from the EAR5 reanalysis data. The data were detrended over 1950–2017.

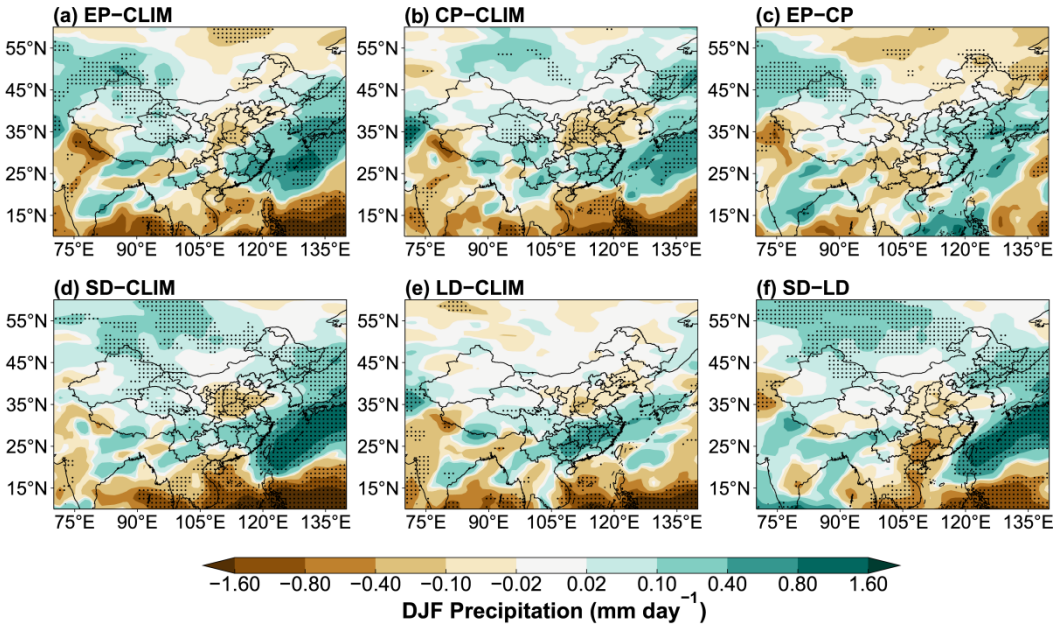

Figure S5. Composite differences in DJF mean precipitation (mm day^{-1}) between EP and CLIM in (a), CP and CLIM in (b), EP and CP in (c), SD and CLIM in (d), LD and CLIM in (e), and SD and LD in (f). The stippled areas indicate statistical significance with 90% confidence from a two-tailed T-test.

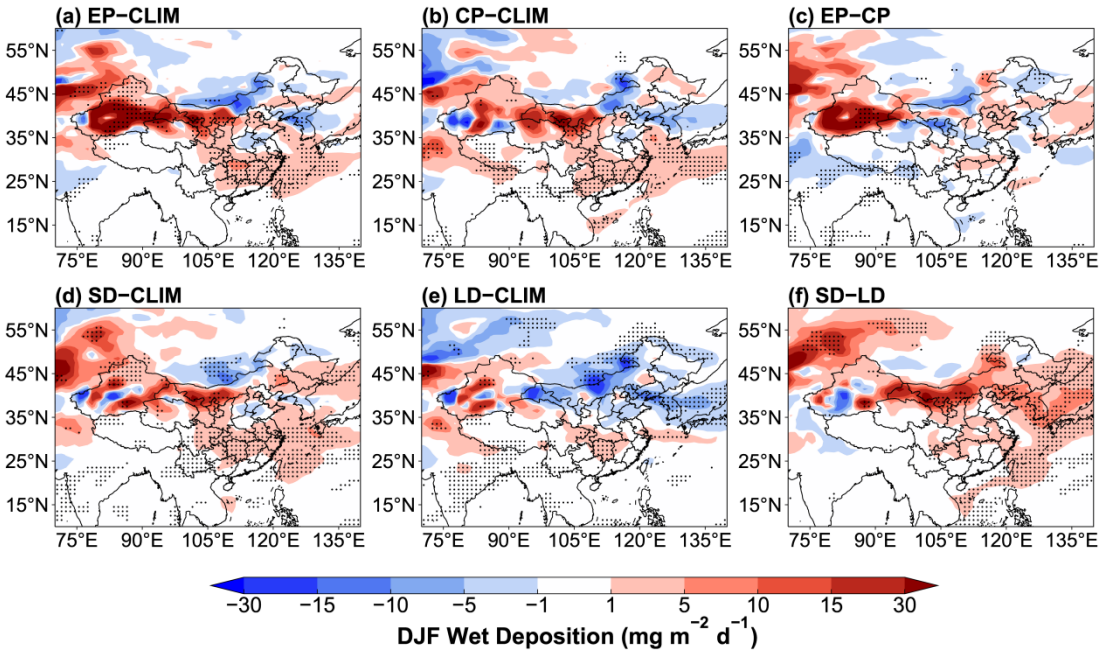

Figure S6. Composite differences in DJF mean dust wet deposition (mg m^{-2} d^{-1}) between EP and CLIM in (a), CP and CLIM in (b), EP and CP in (c), SD and CLIM in (d), LD and CLIM in (e), and SD and LD in (f). The stippled areas indicate statistical significance with 90% confidence from a two-tailed T-test.

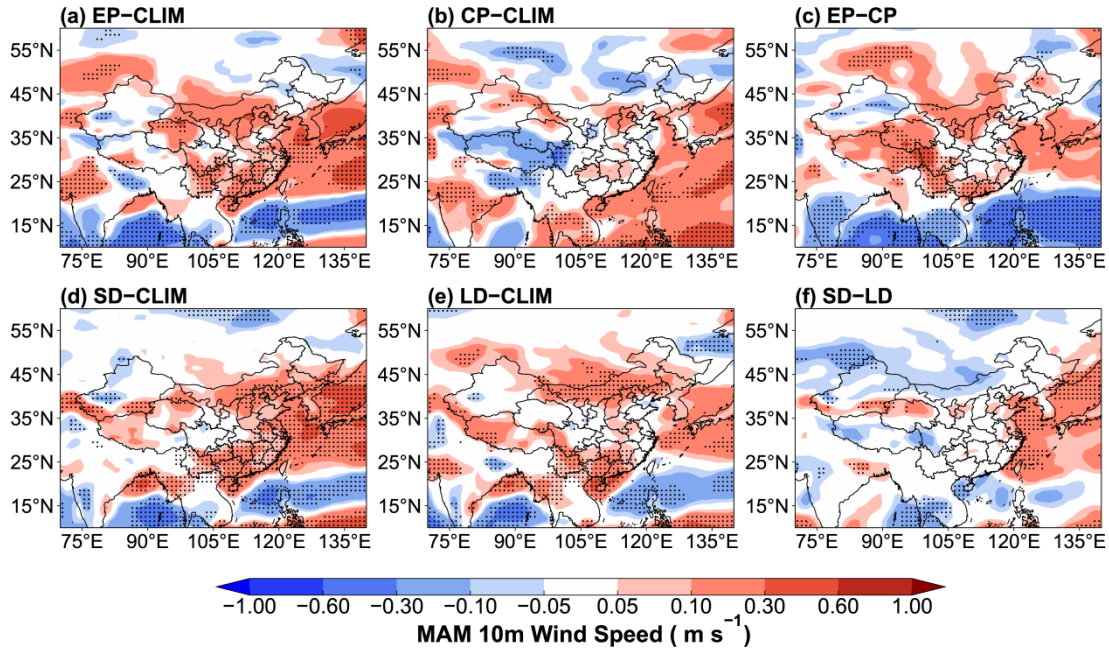

Figure S7. Composite differences in MAM mean 10-m wind speed (m s^{-1}) between EP and CLIM in (a), CP and CLIM in (b), EP and CP in (c), SD and CLIM in (d), LD and CLIM in (e), and SD and LD in (f). The stippled areas indicate statistical significance with 90% confidence from a two-tailed T-test.

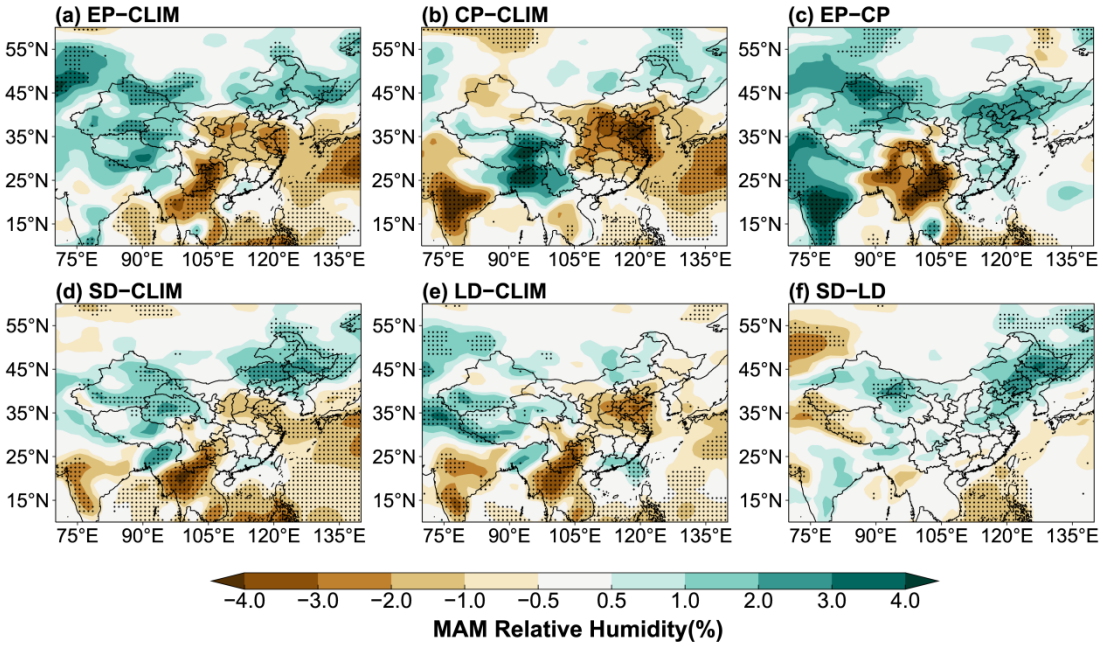

Figure S8. Composite differences in MAM mean relative humidity (units: %) between EP and CLIM in (a), CP and CLIM in (b), and EP and CP in (c), SD and CLIM in (d), LD and CLIM in (e), and SD and LD in (f). The stippled areas indicate statistical significance with 90% confidence from a two-tailed T-test.

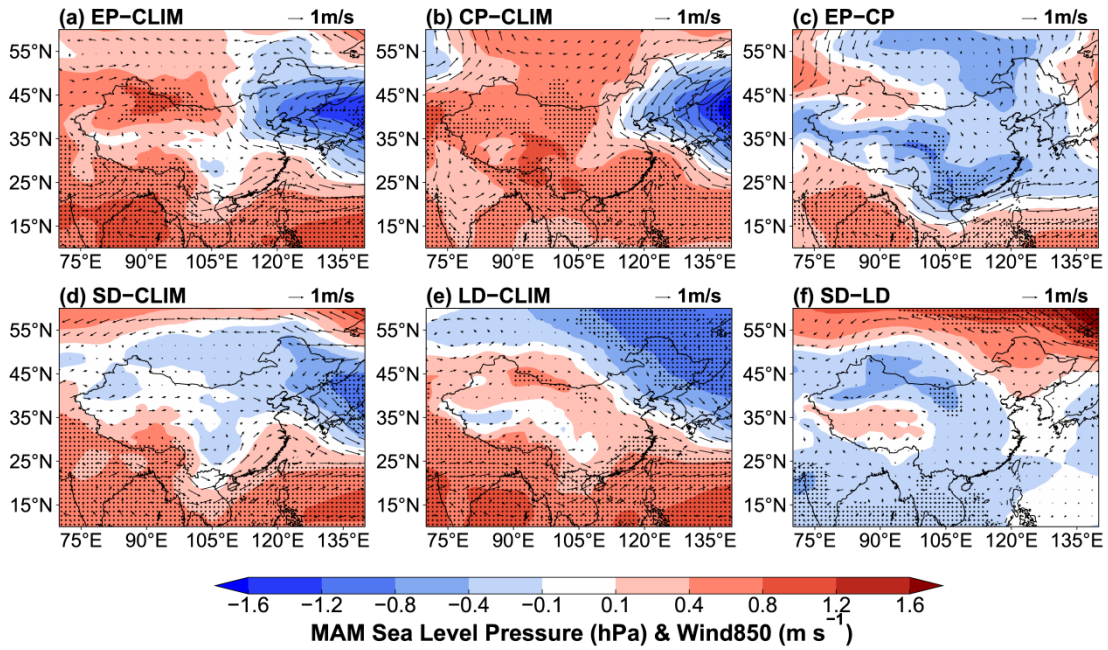

Figure S9. Composite differences in MAM mean sea level pressure (SLP, shaded; units: hPa) and wind at 850 hPa (WIND850, vector; units: m s^{-1}) between EP and CLIM in (a), CP and CLIM in (b), and EP and CP in (c), SD and CLIM in (d), LD and CLIM in (e), and SD and LD in (f). The stippled areas indicate statistical significance with 90% confidence from a two-tailed T-test.

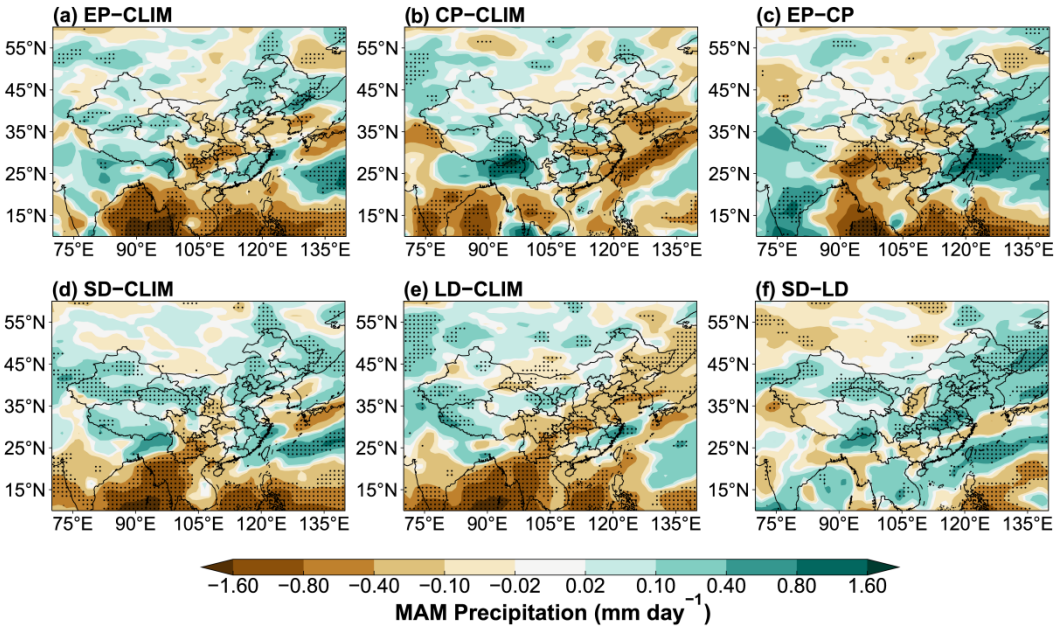

Figure S10. Composite differences in MAM mean precipitation (mm day^{-1}) between EP and CLIM in (a), CP and CLIM in (b), EP and CP in (c), SD and CLIM in (d), LD and CLIM in (e), and SD and LD in (f). The stippled areas indicate statistical significance with 90% confidence from a two-tailed T-test.

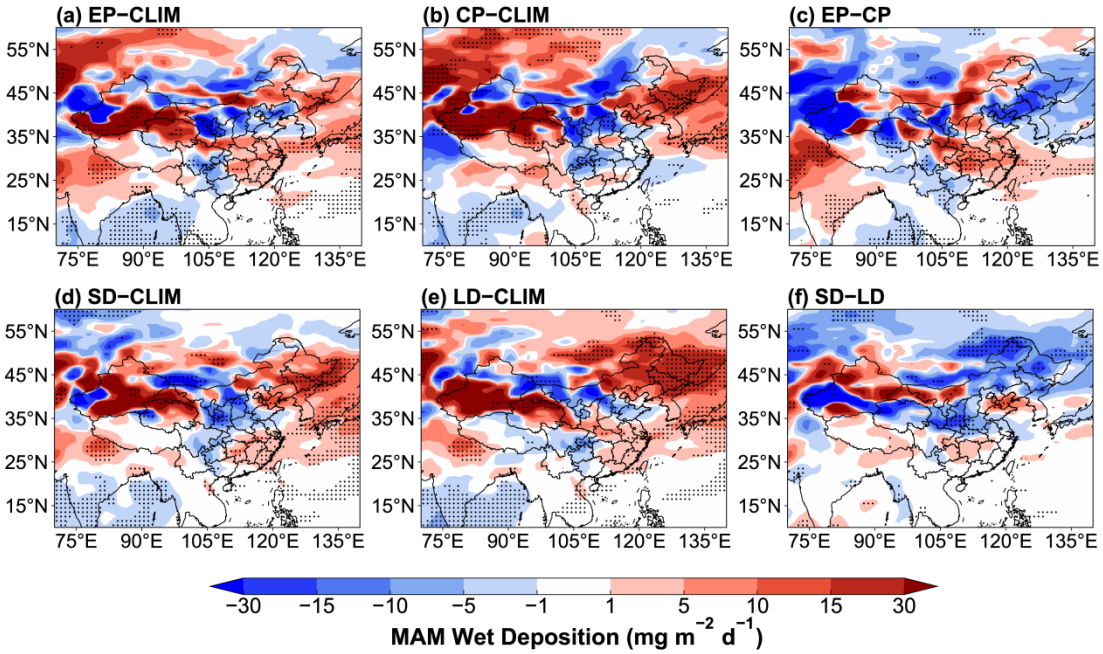

Figure S11. Composite differences in MAM mean dust wet deposition (mg m^{-2} d^{-1}) between EP and CLIM in (a), CP and CLIM in (b), EP and CP in (c), SD and CLIM in (d), LD and CLIM in (e), and SD and LD in (f). The stippled areas indicate statistical significance with 90% confidence from a two-tailed T-test.

References:

Guo, Y., and Tan, Z.: Westward migration of tropical cyclone rapid-intensification over the Northwestern Pacific during short duration El Nino, Nat. Commun., 9, 1507, https://doi.org/10.1038/s41467-018-03945-y, 2018.

Kao, H., and Yu, J.: Contrasting Eastern-Pacific and Central-Pacific Types of ENSO, J. Clim., 22, 615–632, https://doi.org/10.1175/2008JCLI2309.1, 2009.

Yu, X., Wang, Z., Zhang, H., He, J., and Li, Y.: Contrasting impacts of two types of El Niño events on winter haze days in China's Jing-Jin-Ji region, Atmos. Chem. Phys., 20, 10279–10293, https://doi.org/10.5194/acp-20-10279-2020, 2020.

Yuan, Y., and Yang, S.: Impacts of Different Types of El Niño on the East Asian Climate: Focus on ENSO Cycles, J. Clim., 25, 7702–7722, https://doi.org/10.1175/JCLI-D-11-00576.1, 2012.